CCFE-PR(17)71

D.R. Mason, D. Nguyen-Manh, and C.S. Becquart

An empirical potential for simulating vacancy clusters in tungsten

Enquiries about copyright and reproduction should in the first instance be addressed to the Culham Publications Officer, Culham Centre for Fusion Energy (CCFE), Library, Culham Science Centre, Abingdon, Oxfordshire, OX14 3DB, UK. The United Kingdom Atomic Energy Authority is the copyright holder.

An empirical potential for simulating vacancy clusters in tungsten

D.R. Mason[1], D. Nguyen-Manh[1], and C.S. Becquart[2]

[1]CCFE, Culham Centre for Fusion Energy, Abingdon, Oxfordshire OX14 3DB, United Kingdom
[2]UMET, UMR 8207, Université Lille I, F-59655 Villeneuve d'Ascq, France

Further reproduction distribution of this paper is subject to the journal publication rules.

An empirical potential for simulating vacancy clusters in tungsten

D.R. Mason*[1], D. Nguyen-Manh[1], and C.S. Becquart[2]

[1]CCFE, Culham Centre for Fusion Energy, Abingdon, Oxfordshire OX14 3DB, United Kingdom
[2]UMET, UMR 8207, Université Lille I, F-59655 Villeneuve d'Ascq, France

August 9, 2017

Abstract

We present an empirical interatomic potential for tungsten, particularly well suited for simulations of vacancy-type defects. We compare energies and structures of vacancy clusters generated with the empirical potential with an extensive new database of values computed using Density Functional Theory, and show that the new potential predicts low-energy defect structures and formation energies with high accuracy. A significant difference to other popular embedded atom empirical potentials for tungsten is the correct prediction of surface energies. Interstitial properties and short-range pairwise behaviour remain similar to the Ackford-Thetford potential on which it is based, making this potential well-suited to simulations of microstructural evolution following irradiation damage cascades. Using atomistic kinetic Monte Carlo simulations, we predict vacancy cluster dissociation in the range 1100-1300K, the temperature range generally associated with stage IV recovery.

1 Introduction

High-purity tungsten has some exceptional physical properties. As well as being a refractory metal with the highest elemental melting point (3690K), it has the lowest coefficient of thermal expansion, and very high thermal conductivity. Combined with its high resistance to sputtering, and the fact that under fusion neutron irradiation its transmutation products are considered acceptable [1, 2], these qualities have lead to its choice as a material for the ITER divertor[3, 4, 5]. However, tungsten is brittle, and its thermomechanical properties become

*daniel.mason@ukaea.uk

worse on irradiation [6, 7, 8], so a key aim of fusion materials research is to understand the atomistic processes of irradiation damage generation, and how the accumulation of such damage acts as an impedence to dislocation motion and hence a reduction in plasticity.

After the initial high-energy generation of defects by radiation cascade damage, the underlying processes governing defect cluster interactions will be due to by small adjustments of chemical bonds for atoms in non-perfect-crystal arrangements. Density functional theory, with appropriate choice of functional used, is the standard workhorse for calculating these changes in electronic bonding[9]. But the microstructural evolution driven by the competition between these subtle energy differences and configurational entropy emerges in systems of many thousands of atoms, and over timescales of years. Empirical potentials are therefore still routinely required for simulations of collective dynamic behaviours, and will continue to be so as computing power brings into range ever more ambitious molecular dynamics and kinetic Monte Carlo simulations.

Work on the new empirical parameterization presented here was motivated by conflicting experimental and theoretical observations on vacancy-type dislocation loops generated by self-ion-irradiation of ultra-high-purity tungsten foil. In 2008, Gilbert et al.[10] computed the relative stability of nanoscale vacancy-type defects in tungsten, and concluded that voids would be the most stable configuration of vacancies. They also showed, using a potential by Derlet et al[11] that small vacancy type dislocation loops (diameter <3.5nm) were unstable with respect to transformation to void plates. Sand et al. showed that molecular dynamics simulations of radiation damage cascades in bulk tungsten[12], and in foil[13] produced rather diffuse vacancy-rich regions, and interstitial-type dislocation loops. By contrast, experiments by Jäger and Wilkens[14] and subsequently *in situ* TEM studies of self-ion-irradiation of ultra-high-purity tungsten foils by Yi et al. [15, 16, 13] have shown that stable nanoscale vacancy loops are indeed generated in radiation damage cascades; in fact they may be as numerous as interstitial type loops.

In section 2 we show that the principal problem with the earlier potentials was a low surface energy, and that this may be increased without significantly affecting near-equilibrium properties by adjusting the embedding function. In section 3 we discuss vacancy clusters in pure tungsten in detail, and provide dozens of new *ab initio* calculations which are used as a database to prove our new parameterization. Finally we perform atomistic kinetic Monte Carlo simulations in section 4, which show that the characteristic dissociation temperature for vacancy clusters is in the stage IV recovery range 1100-1300K, and compare our results to recent experiments by Ferroni et al.[17]

2 A modified Finnis-Sinclair potential for tungsten

The Finnis-Sinclair (FS) family[18] of embedded atom empirical potentials are a popular starting point for atomistic simulation. Their longevity is due to their transferability, which in turn is thanks to their simple form- analytic and (largely) smooth in its derivatives. They are also somewhat underfitted, reproducing lattice parameters and elastic constants, rather than intricate defect properties.

In this development of the tungsten potential, we introduce smoothly-varying, physically-motivated corrections to the original FS form. Each correction improves a desired physical property almost independently, so while many additional parameters are presented, their fitting was not onerous, nor are the physical properties presented in section 3 especially sensitive to their values.

For an embedded atom potential, the energy of atom i is written as

$$E_i = {}^1\!/_2 \sum_{j \neq i} V\left(r_{ij}\right) + F\left[\rho_i\right], \tag{1}$$

where $V\left(r\right)$ is a pairwise potential energy, repulsive at short range, and $F\left[\rho\right]$ an embedding function for an atom in a region of electron density ρ, given by

$$\rho_i = \sum_{j \neq i} \phi\left(r_{ij}\right). \tag{2}$$

Our modifications will will be piecewise polynomial additions to the functional forms of $V\left(r\right)$ and $F\left[\rho\right]$, and not add new terms to equation1.

2.1 Surface energy and void formation energy

A well-known issue with embedded atom potentials for bcc metals is the underestimation of surface energies[19]. A related issue for tungsten potentials is the overestimation of the vacancy cluster binding energies. Both contain atoms in low-electron-density regions, so it is on this region we focus. The atoms around a vacancy cluster do not significantly relax, so there is little freedom to improve the radial terms $V\left(r\right)$ or $\phi\left(r\right)$. Instead it must be that the embedding function is overestimating the binding energy where the electron density ρ drops significantly below that in the perfect lattice.

In the second moment approximation and at zero electronic temperature, we write that the embedding energy is directly proportional to the local electron bandwidth, W, i.e. $F\left[\rho\right] \sim W\left[\rho\right]$. At electron densities comparable to the perfect lattice, the bandwidth goes as the square root of the density, $W\left[\rho\right] \sim \sqrt{\rho}$. Where ρ is low, we want to reduce bonding by reducing the bandwidth, so instead consider an affine form- $W\left[\rho\right] = W_0 + W_1\rho$. At very low density we must recover $F\left[\rho = 0\right] = 0$, or the cohesive energy will be changed, so we suggest a polynomial between $\rho = 0$ and the first intercept between affine and square

root forms. We ensure a smooth transition between affine and square root forms at high density with a polynomial interpolation. We therefore have four parameters to fit; two for the affine form and two for the range of the transition to square-root form. The values of these parameters have been linear-least-squares fitted to the DFT values for vacancy clusters of size 2-5[20], and the resulting embedding function is illustrated in figure 1. The full parameterization of the embedding function is given in appendix A.

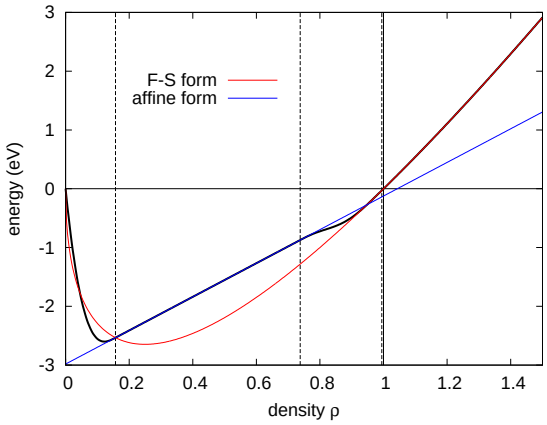

Figure 1: The electronic embedding function plotted against electron density for the modified EAM potential. Note that in the gauge used the equilibrium electron density is $\rho = 1$ and $F[0] = F[1] = 0$. The dashed lines mark transitions between sections of the piecewise form, from left to right ρ_-, ρ_1, ρ_2. These mark the transition from very low density to affine form, and the polynomial switching region from affine to square root form.

2.2 Repulsive potential: long range

The long-range part of the Finnis-Sinclair pairwise potential is discontinuous in its second derivative at the cutoff length. This can lead to unexpected behaviour in lattice statics when comparing vibrational free energy between structures where atoms move across this cutoff. This is remedied by smoothly interpolating to zero between second- and third- nearest neighbours with a 7th order polynomial, with continuous first, second and third derivatives at each end.

The regions between equilibrium neighbour separations are important for interstitial formation energies. Rather than attempting a refit of the interstitial properties, which would necessarily have a knock-on effect on dislocation cores too, we chose a maximum range such that the magnitude of the second derivative is minimised in the interpolation region. Therefore while the long-range correction introduces a new cutoff parameter, it is not empirically fitted. Our

configuration	energy					formation volume				
	DFT	this work	other EAM (a)	(b)	(c)	DFT	this work	other EAM (a)	(b)	(c)
$\langle 111 \rangle_d$	10.086[d]	9.33	10.52	9.46	9.25	1.68[e]	1.57	1.17	1.33	1.57
$\langle 111 \rangle_c$		9.31	10.50	9.46	9.22		1.58	1.10	1.25	1.55
$\langle 110 \rangle_d$	10.545[d]	9.56	10.75	9.78	9.51		1.62	1.67	1.11	1.54
$\langle 100 \rangle_d$	12.200[d]	9.74	12.71	11.67	9.77		1.45	1.34	1.03	1.33
tetrahedral		9.89	11.82	10.93	9.86		1.62	1.58	1.07	1.50
octahedral		9.97	12.49	11.68	9.94		1.50	1.50	1.07	1.36

Table 1: Self-interstitial properties computed for a relaxed 4x4x4 cell (128+1 atoms). Energies in eV, formation volume as fraction of the atomic volume. DFT values from (d) Muzyk et al[20], and (e) Nguyen-Manh & Dudarev[29]. Other empirical potential results computed from analytic forms in (a) Marinica et al[19], (b) Derlet et al[11], (c) Ackland-Thetford[21].

potential returns similar interstitial and dislocation properties to the Ackland-Thetford parameterization.

2.3 Repulsive potential: short range

The short-range part of the Finnis-Sinclair pairwise potential was stiffened by Ackland and Thetford[21] to better describe pairs of atoms in close proximity. It is now conventional for radiation cascade simulations to further stiffen at very-short-range by transitioning smoothly to the universal ZBL pairwise form[22, 23]. We tweak the Ackland-Thetford parameters slightly to better fit DFT data using the method of ref[24]. and transition to ZBL using a polynomial switching function.

Between $r = 2.5\mathring{A}$ and $r = 3.25\mathring{A}$ (covering first and second nearest neighbour separations) there is very little difference between our new parameterization and the Ackland-Thetford form.

3 Results

3.1 DFT calculations

Density functional theory calculations described in this work were performed using the Vienna Ab-initio Simulation Package (VASP) code, with ion-electron interaction implemented using the projector-augmented waves (PAW) method [25, 26, 27]. Exchange and correlation effects were described by the Perdew-Burke-Ernzerhof (PBE) generalized gradient approximation (GGA) [28]. A kinetic energy cutoff of 350eV was used, with 2x2x2 k-points. The calculation cell size used was 5x5x5 cubic bcc cells (250 atoms) unless otherwise stated.

3.2 Point-defect and defect cluster properties

The formation energies and relaxation volumes of the self-interstitials is given in table 1. It should be noted that the cell size used for these calculations is very small, in order to allow the direct comparison with DFT, and there is a significant size effect. At 5x5x5 unit cells, the formation energy of the lowest energy interstitial, the $\langle 111 \rangle_c$ crowdion, falls to 8.99eV, and is only converged fully to 8.94eV at 7x8x9 unit cells (1008+1 atoms).

We present vacancy cluster formation energies and relaxation volumes in table 2. Structures for the vacancy clusters are shown in figure 2. To order vacancy clusters we introduce a single order parameter which indicates the degree of compactness. For a cluster containing N vacancies in a structure with nearest neighbour separation d_0 ($= \sqrt{3/4}a_0$ for b.c.c.), define

$$\chi \equiv \frac{\sum_{i,j>i} \frac{|r_{ij}|^2}{d_0^2}}{\frac{1}{2}N(N-1)}. \tag{3}$$

This takes the minimum value of 1 if all vacancies are nearest neighbours, and is larger for more diffuse structures.

The general trend for empirical potentials is to grossly overestimate the binding energy for vacancy clusters, potentially leading to erroneous conclusions about the readiness to nucleate and grow clusters and voids in a vacancy-rich region. As a single comparable number across potentials we consider the nearest neighbour divacancy (2v1). Our DFT calculations suggest the nearest neighbour divacancy binding energy is very slightly positive at 0.048eV. There is some considerable debate about the direct experimental estimate of the divacancy binding energy by Park et al[32], 0.7eV, owing to the (necessarily) rather small sample taken in the FIM study. A small concentration of carbon impurities in the experimental sample may also have greatly increased the probability of finding divacancies. We should therefore prefer to rely on the DFT calculation as our reference.

The EAM-type potentials CEA-4,DND and AT give strong divacancy binding at $0.518, 0.567$ and 0.432eV respectively. The bond-order potential of Ahlgren et al[33] is slightly higher at $0.656\text{eV}/\text{Å}^2$, as is the MEAM potential of Zhang et al[34](0.580eV). Our potential stands alone with a good estimate of the nearest neighbour binding energy of 0.170eV. We believe our potential is also the only one to have negative binding energies for the second- and third- neighbour divacancies. A summary of vacancy cluster results is given in table 2.

3.3 Transition energies

Computed transition energies are given in table 3. To generate a statistically comparable result between EAM potentials we considered a larger set of 33 transitions for 1-4 vacancy clusters, namely forward and backward transitions 1v1x1', 2v1x2, 2v1x3, 2v1x5, 2v2x4, 2v3x4, 2v5x4, 3v1x1', 3v1x2, 3v1x3, 3v1x5, 3v2x3, 3v2x5, 3v4x5, 3v5x5', 3v5x6, 4v1x2, 4v1x3. The results are also presented as a scatter plot in figure 3, including more transitions for clusters up

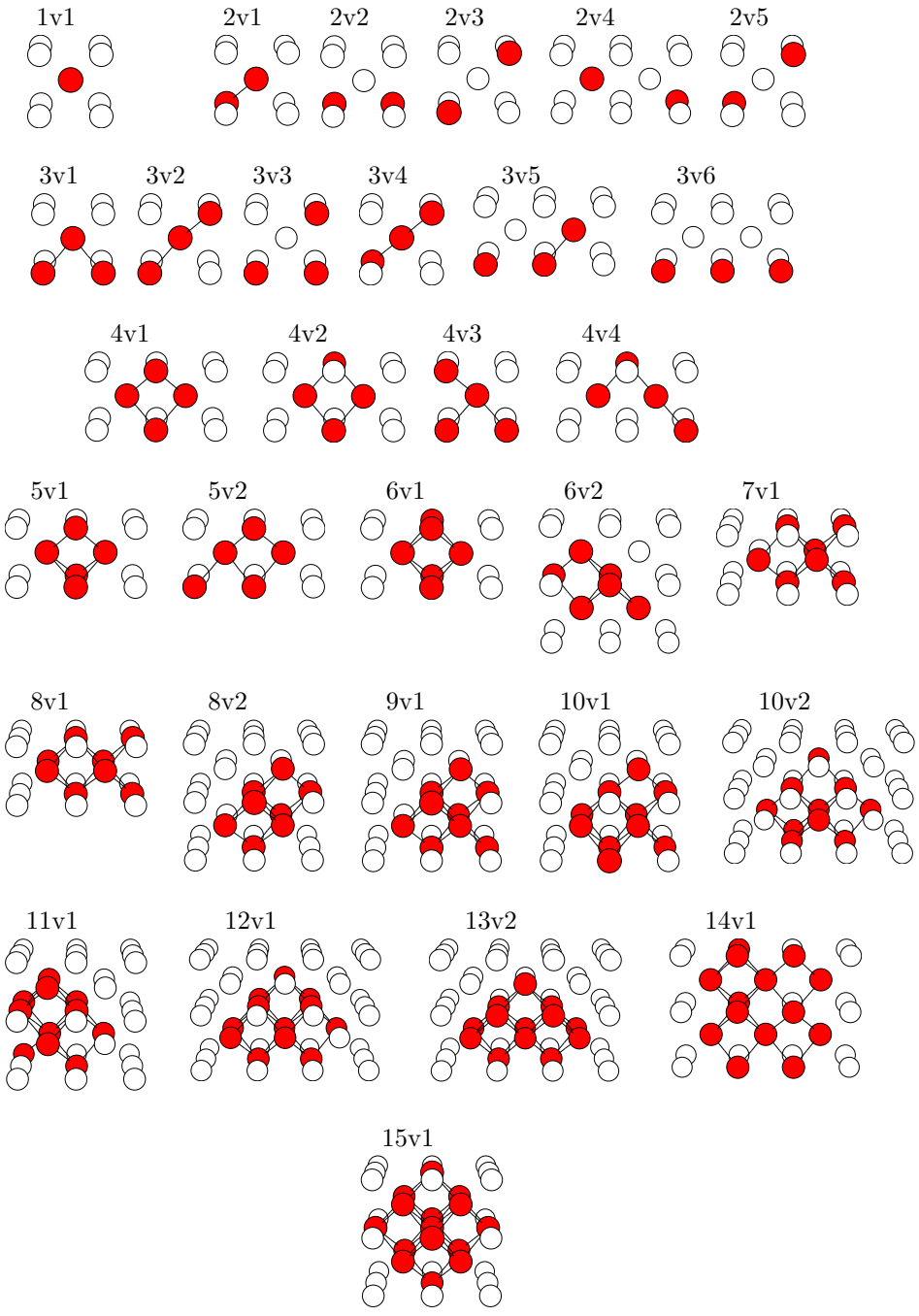

Figure 2: The 31 vacancy cluster configurations considered here.

vacancy cluster	degeneracy	cluster param χ	energy DFT	energy EAM	relax vol DFT	relax vol EAM
1v1	1		3.619	3.727		-0.36
2v1	4	1.00000	0.048	0.170		-0.86
2v2	3	1.33333	-0.286	-0.130		-1.00
2v3	6	2.66667	-0.063	-0.337		-0.85
2v4	12	3.66667	0.042	-0.061		-0.82
2v5	4	4.00000	-0.094	-0.141		-0.77
3v1	12	1.11111	0.311	0.433		-1.31
3v2	12	1.55556	0.074	0.058		-1.29
3v3	12	1.77778	-0.257	-0.468		-1.47
3v4	4	2.00000	0.153	0.386		-1.34
3v5	24	2.00000	-0.047	0.006		-1.50
3v6	3	2.66667	-0.348	-0.177		-1.76
4v1	6	1.11111	1.156	1.446		-1.63
4v2	6	1.33333	0.900	1.059		-1.54
4v3	24	1.38889	0.590	0.674		-1.65
4v4	24	2.00000	0.595	0.310		-1.70
5v1	12	1.26667	2.108	2.494		-1.91
5v2	48	1.53333	1.318	1.694		-1.98
6v1	3	1.33333	3.340	3.945		-2.32
6v2	24	1.48889	3.072	3.541		-2.18
7v1	24	1.58730	4.305	4.996		-2.59
8v1	6	1.71429	5.523	6.463		-3.04
8v2	4	1.71429	5.992	6.422		-2.48
9v1	24	1.85185	7.237	7.883		-2.89
10v1	48	2.03704	7.657	9.356		-3.32
10v2	48	2.09630	8.194	8.953		-3.17
11v1	48	2.19394		10.784		-3.63
12v1	48	2.26263		12.652		-3.77
13v1	24	2.43590		14.143		-4.25
14v1	48	2.88645		15.578		-4.60
15v1	1	2.28571		20.025		-3.77

Table 2: Energy and relaxation volume of vacancy cluster configurations (see also figure 2). The formation energy of the monovacancy is given, then subsequently the binding energies for the ath cluster containing N vacancies defined as $E_b(N,a) = NE^f(1) - E^f(N,a)$. Energies are given in eV, relaxation volume in fraction of atomic volume. Other empirical potential results are given in the text. The order parameter χ is defined in equation 3. Self-consistent experimental estimates for the monovacancy formation energy are 3.61 ± 0.07[30] to 3.77 ± 0.07[31].

	DFT	this work	other EAM (a)	(b)	(c)	Kang-Wienberg[35]
1v1x1'	1.756	1.523	2.056	1.845	1.449	1.750
2v1x2	0.069	0.113	0.362	0.191	0.017	0.150
2v1x3	0.051	0.366	0.289	0.482	0.316	0.253
2v1x5	-0.039	-0.054	0.010	0.097	0.045	0.155
3v1x1'	-0.610	0.079	0.492	0.314	-0.023	0.605
3v1x2	-0.115	0.279	0.332	0.626	0.376	0.188
3v1x3	0.337	0.456	0.543	0.617	0.353	0.451
3v1x5	0.133	0.064	0.340	0.200	0.030	0.213
4v1x3	0.105	0.525	0.645	0.808	0.476	0.386
error		-0.21 ± 0.05	0.48 ± 0.07	0.30 ± 0.07	-0.24 ± 0.05	0.04 ± 0.03

Table 3: Vacancy cluster transition energies. The transition nvaxb takes an n-vacancy cluster from structure a to structure b (see figure 2). Other empirical potential results have been computed from analytic forms in (a) Marinica et al[19], (b) Derlet et al[11], (c) Ackland-Thetford[21]. In order to better show the differences in the migration energy, the value for the monovacancy migration energy is given in eV, then subsequent columns show the difference, ie the total DFT 2v1x2 migration barrier is 1.756+0.069=1.825eV. The simple K-W model is $E_s = (E_1 + E_2)/2 + 1.75$. A generally accepted experimental range for the $1v1x1'$ monovacancy migration energy is 1.68 ± 0.06eV at 1550K rising to 2.02 ± 0.05eV at 2600K[36]. Experiments suggest divacancy migration energies should be similar to that of the monovacancy[32, 37]. Note that the error computed excludes the special case of trivacancy migration energy.

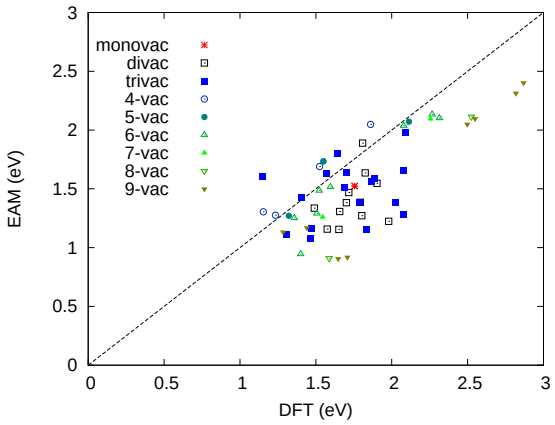

Figure 3: Transition energies comparing the EAM potential described here with the DFT computed values using the method described in the text. Other EAM potentials give similar scatter plots; a statistical comparison is given in the text.

to size 9. We find that the EAM potentials perform similarly well. Our potential gives similar results to AT, slightly underestimating the barriers, whereas CEA-4 and DND slightly overestimate the barriers.

The benchmark figure for comparing vacancy cluster transitions must be the monovacancy migration energy, but it is clear that performing well in this metric alone is insufficient for deciding a good potential for vacancy dynamics. One transition merits special attention. The trivacancy may rapidly diffuse without dissociation purely through nearest neighbour atom-vacancy exchanges. The DFT nudged-elastic-band calculation finds the saddle point to be a very high symmetry configuration, with four vacant sites tetrahedrally distributed around the migrating atom. This unusual bonding configuration allows for a very low energy migration path. The empirical potentials do not find this high-symmetry, low-energy saddle, and so greatly overestimate the tri-vacancy migration energy. An examination of the bond lengths and electron density for the participating atoms suggests that the the energy of this special saddle point can not be reproduced by modifying the EAM form- it is an example of a situation where angular dependent bonding terms are necessary.

It is also worth noting that the Kang-Weinberg (K-W) model[35], $E_s \approx (E_1 + E_2)/2 + \Delta E$, yields good saddle points. The magnitude of the barrier ΔE can easily be tweaked to exactly reproduce the average saddle point barrier; more importantly we see that the spread of the errors (defined as the difference between DFT and empirical result) introduced by this estimate is smaller than that for the EAM potentials. This implies that this very simple saddle point model is a *better* estimate than that of the EAM potentials.

3.4 Surface properties

The surface energy, and interlayer relaxations are important quantities for any simulations which include explicit crystal surfaces, or where voids are of sufficient size that they start to resemble free surfaces locally. Empirical potentials for tungsten have struggled to reproduce these fundamental quantities, adding a layer of uncertainty to results from thin-foil simulations. The (110) surface has the lowest energy for many bcc metals, including tungsten. Experimentally the (110) surface energy has been determined to be $0.23\text{eV}/\text{Å}^2$[38] which coincides well with its DFT-computed value $0.250\text{eV}/\text{Å}^2$[39]. Empirical potentials give significantly (40% or more) lower values. Although the trend from one surface to the next may be adequately reproduced[19], this gross underestimate means additional surface in the form of voids, or surface roughness is far too readily formed. The EAM-type potentials CEA-4,DND and AT give similar results- $0.156, 0.150$ and 0.161 respectively. The bond-order potentials of Mrovec et al[40], and Ahlgren et al[33] are no better, giving 0.167 and $0.135\text{eV}/\text{Å}^2$ respectively. Juslin et al[41] report $0.09\text{eV}/\text{Å}^2$ for the (100) surface, which should be higher energy. Our explicit modification of the low-electron-density binding stands alone with an excellent answer of $0.218\text{eV}/\text{Å}^2$. Results are summarised in table 4.

For the (100) surface, our EAM potential produces only the $p(1 \times 1)$ periodicity structure, observed in pure tungsten above room temperature[42], and does not generate the $(\sqrt{2} \times \sqrt{2})R45^\circ$ unit cell with *p2mg* symmetry seen at low temperature and using DFT[42, 43]. In the (111) orientation, the surface appears as a hexagonal cell with $(a = \sqrt{2}a_0, c = \sqrt{\frac{3}{4}}a_0)$ and atoms at $(0,0,0), (\frac{1}{3}, \frac{1}{3}, \frac{1}{3}), (\frac{2}{3}, \frac{2}{3}, \frac{2}{3})$. A slightly lower energy surface (by $2\text{meV}/\mathring{A}^2$) was found with the EAM potential if the top layer was only half filled, ie a $c(1 \times 2)$ reconstruction with atoms at $(0,0,0)$ and $(1,0,0)$ removed. The (110) and (211) surfaces did not show any reconstructions with the EAM potential.

3.5 Vacancy formation energies and transitions at surfaces

Using the EAM potential we have investigated the formation energy of vacancies near the surfaces, and computed the transition energies for vacancy movement to and from the surface. The supercells used for the calculations were of cuboidal shape, containing about 2000 atoms, and allowed to relax in the direction normal to the surface only. Transitions were computed using the drag method[44], with care taken to identify any metastable states and to ensure smooth paths between replicas. The results are summarised in figure 4.

The following features can be noted as common to all surfaces: The formation energy is low for a vacancy in the surface layers, but rapidly reaches the bulk level by two lattice parameters depth. The vacancy migration energy is also at its bulk level beyond this depth. Strings of atoms can be readily displaced along [111] directions, which can destabilise a vacancy immediately below the surface.

surface	energy						layer relaxation				
	DFT	this work	other EAM (a)	other EAM (b)	other EAM (c)		DFT	this work	other EAM (a)	other EAM (b)	other EAM (c)
(110)	0.250	0.218	0.156	0.150	0.161	δ_{12}	-3.6	-3.05	-1.13	-0.96	-2.36
						δ_{23}	0.2	0.07	0.02	0.02	0.26
						δ_{34}		0.00	0.00	0.00	0.20
(100)	0.290	0.239	0.183		0.182	δ_{12}	-6	-2.76	-0.63		-1.19
						δ_{23}	0.5	-0.56	-0.61		-2.96
						δ_{34}		0.23	0.22		1.42
(111)	0.278	0.257	0.200	0.193	0.206	δ_{12}		-4.48	-4.89	-6.22	-4.40
						δ_{23}		-14.87	-7.48	-10.22	-12.72
						δ_{34}		7.49	4.96	8.34	9.68
(211)	0.261	0.241	0.186		0.190	δ_{12}		-7.92	-4.85		-5.80
						δ_{23}		0.21	1.06		0.95
						δ_{34}		-2.57	-0.89		-1.03

Table 4: Unreconstructed surface properties. Energies in eV/Å^2. Layer relaxation in % ($\delta_{ij} = 100\% \times \left(\frac{(\bar{z}_i - \bar{z}_j)}{(z_i^0 - z_j^0)} - 1\right)$, where $\bar{z}_i$ is the average position of an atom in the ith layer, and z_i^0 the perfect lattice position. DFT values from ref [39]. Other empirical potential results computed from analytic forms in (a) Marinica et al[19], (b) Derlet et al[11], (c) Ackland-Thetford[21]. The experimental estimate for the surface energy is 0.229eV/Å^2[38].

A few metastable reconstructions were identified for vacancies immediately below the surface (see figure 4 insets).

4 Dissociation of vacancy clusters

We have investigated the dissociation of existing vacancy clusters using the EAM potential and lattice-based atomistic kinetic Monte Carlo. In section 3.3, we concluded that it was better to use a Kang-Wienberg model barrier between two competing vacancy clusters (the average energy of the competing states plus a constant), rather than to compute the barrier using the nudged elastic band method[44] or similar.

We find that whether transitions are considered between elastically relaxed states, or atoms on a rigid lattice, makes a negligible impact on dissociation times. We attribute this to there being no deep elastic minima in the potential energy landscape- a different conclusion would surely be reached if a second phase[45] or interstitial clusters[46] were present. To ensure this methodology is consistent with with the migration pathways found in section 3.5, we searched for metastable off-lattice rearrangements for single vacancies near the surface of the 15 vacancy cluster, but found none.

We used the standard n-fold way kinetic Monte Carlo algorithm[47] considering all vacancy-atom exchanges each time step, with a K-W model rate for

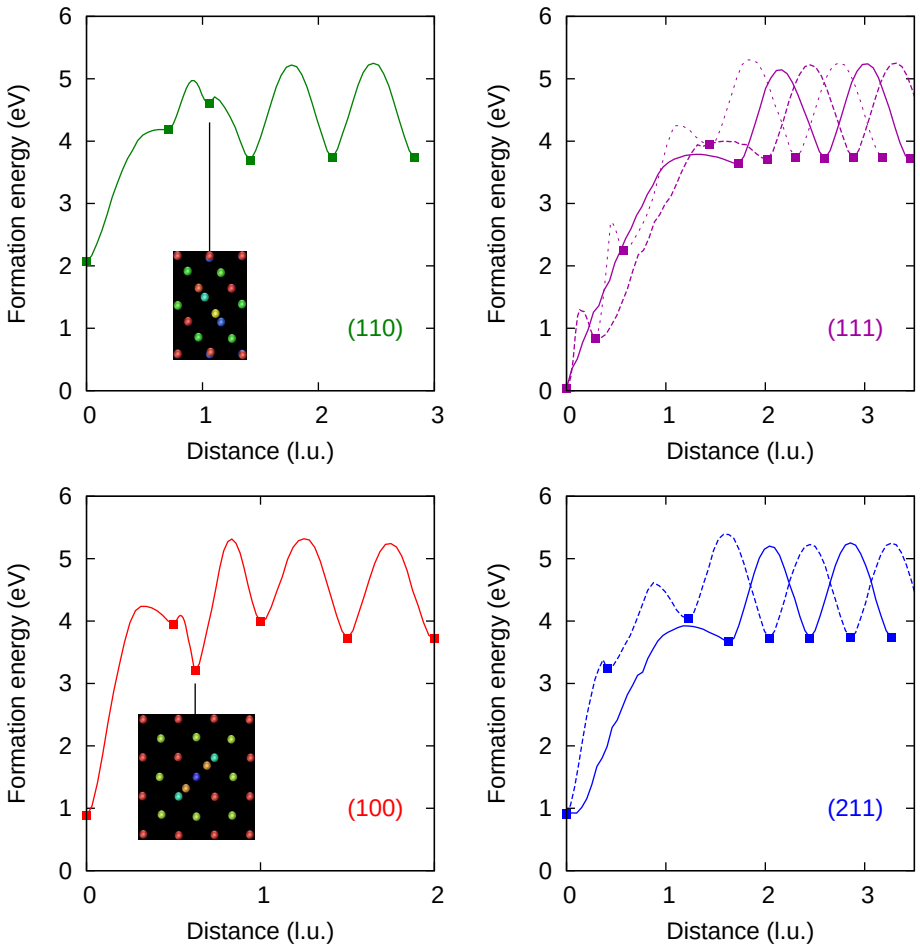

Figure 4: Formation energy and transition paths for a single vacancy brought close to a surface using the EAM potential. Insets show reconstructions with atoms colour-coded by depth, (red=layer 1, green=layer 2, blue=layer3).

exchange:

$$r_{1\to 2} = \nu_D \exp\left(-\frac{(E_2 - E_1)/2 + \Delta E}{k_B T}\right), \tag{4}$$

where $\nu_D = 6.45 \times 10^{12}$Hz[48] is the Debye frequency and $\Delta E = 1.75$eV. The initial configuration was $13 \times 14 \times 15$ unit cells, with the lowest energy vacancy cluster placed in the centre, and dissociation was deemed to have occured when one or more vacancies separated from the central cluster for 100 steps. The dissociation time was computed at a range of temperatures, and from this a single characteristic temperature for dissociation after one second was found by

Arrhenius fitting. The results are shown in figure 5.

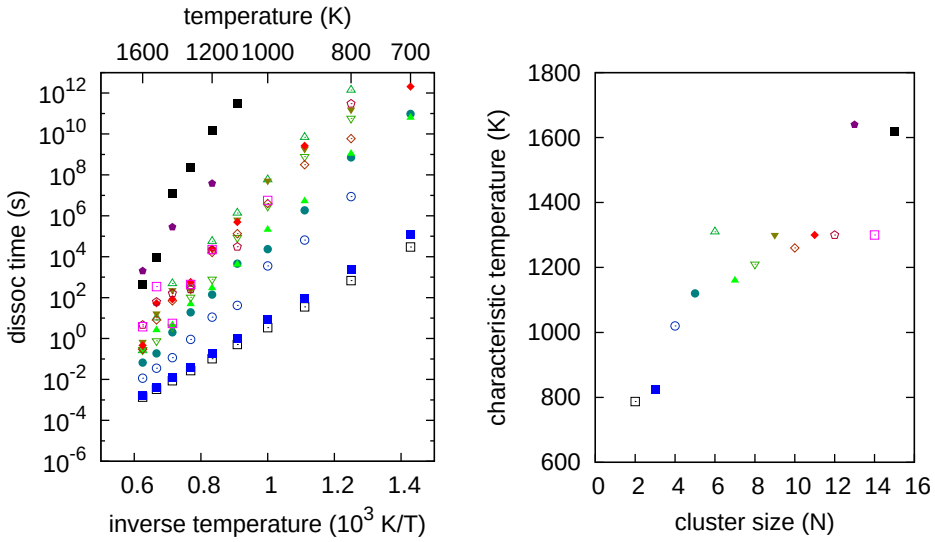

Figure 5: (Left) Average vacancy cluster dissociation time and (right) characteristic temperature for dissociation computed by atomistic Kinetic Monte Carlo simulation as described in the text. The symbols on the left-hand plot correspond to the sizes indicated in the right-hand plot.

5 Conclusions

We have demonstrated a failure of existing empirical potentials to reproduce the properties of tungsten in low-electron-density regions, and have remedied this by stiffening the embedding function. Our potential reproduces experimental properties of monovacancies in tungsten, with a formation energy 3.73eV lying in the experimental range 3.61 ± 0.07[30] to 3.77 ± 0.07[31]. The monovacancy migration barrier (1.52eV) is low compared to the established DFT estimate 1.76eV, but is not unreasonable given the lowest temperature experimental estimate is 1.68 ± 0.06eV[36] taken at 1550K. We have shown in section 3.3 that vacancy cluster transitions are generally well reproduced by a very simple fixed-barrier model for the saddle point energy, but that the energy of individual transitions requires a more sophisticated model of electronic bonding than EAM. We note that the trivacancy has a very low migration energy (1.146eV compared to monovacancy 1.756eV), as it may migrate without cluster dissociation through a very high symmetry saddle.

The divacancy binding energy with the potential detailed here is 0.17eV,

which is a good match to the DFT value 0.05eV. We have shown that this potential reproduces the relative energy of competing vacancy clusters with high fidelity. The binding energy of a low energy n-vacancy cluster varies as $n^{2/3}$- suggesting the surface energy is the dominant factor.

The (110) surface energy for this potential is 0.218 eV/Å^2, which compares well to the experimental value 0.229eV/Å^2[38]. We have shown that the potential developed here predicts vacancies are metastable two lattice parameters below the surface, but if they come closer then that it is possible for strings of atoms to shift along $\langle 111 \rangle$ directions, just as crowdions move, and occasionally generate complex metastable rearrangements with off-lattice atomic positions. However, as these states have very low barriers for a second rearrangement where the vacant site ends up on the surface and near-perfect lattice below, we don't expect these states have a significant effect on microstructural evolution.

We believe our potential stands alone in the quality of its surface and vacancy properties.

6 Acknowledgements

This work has been carried out within the framework of the EUROfusion Consortium and has received funding from the Euratom research and training programme 2014-2018 under grant agreement No 63305, and from the RCUK Energy Programme [grant number EP/P012450/1]. The views and opinions expressed herein do not necessarily reflect those of the European Commission. To obtain further information on the data and models underlying this paper please contact PublicationsManager@ccfe.ac.uk.

References

[1] M.R. Gilbert and J.-Ch. Sublet. Neutron-induced transmutation effects in W and W-alloys in a fusion environment. *Nuclear Fusion*, 51(4):043005, 2011.

[2] M.R. Gilbert, S.L. Dudarev, S. Zheng, L.W. Packer, and J.-Ch. Sublet. An integrated model for materials in a fusion power plant: transmutation, gas production, and helium embrittlement under neutron irradiation. *Nuclear Fusion*, 52(8):083019, 2012.

[3] M. Rieth, J.L. Boutard, S.L. Dudarev, T. Ahlgren, S. Antusch, N. Baluc, M.-F. Barthe, C.S. Becquart, L. Ciupinski, J.B. Correia, C. Domain, J. Fikar, E. Fortuna, C.-C. Fu, E. Gaganidze, T.L. Galn, C. Garca-Rosales, B. Gludovatz, H. Greuner, K. Heinola, N. Holstein, N. Juslin, F. Koch, W. Krauss, K.J. Kurzydlowski, J. Linke, Ch. Linsmeier, N. Luzginova, H. Maier, M.S. Martnez, J.M. Missiaen, M. Muhammed, A. Muoz, M. Muzyk, K. Nordlund, D. Nguyen-Manh, P. Norajitra, J. Opschoor, G. Pintsuk, R. Pippan, G. Ritz, L. Romaner, D. Rupp, R. Schublin,

J. Schlosser, I. Uytdenhouwen, J.G. van der Laan, L. Veleva, L. Ventelon, S. Wahlberg, F. Willaime, S. Wurster, and M.A. Yar. Review on the EFDA programme on tungsten materials technology and science. *Journal of Nuclear Materials*, 417(13):463 – 467, 2011. Proceedings of ICFRM-14.

[4] M. Rieth, S.L. Dudarev, and S.M. Gonzalez de Vicente et al. Recent progress in research on tungsten materials for nuclear fusion applications in Europe. *Journal of Nuclear Materials*, 432(13):482 – 500, 2013.

[5] H Bolt, V Barabash, G Federici, J Linke, A Loarte, J Roth, and K Sato. Plasma facing and high heat flux materials needs for ITER and beyond. *Journal of Nuclear Materials*, 307311, Part 1:43 – 52, 2002.

[6] D.E.J. Armstrong, C.D. Hardie, J.S.K.L. Gibson, A.J. Bushby, P.D. Edmondson, and S.G. Roberts. Small-scale characterisation of irradiated nuclear materials: Part II nanoindentation and micro-cantilever testing of ion irradiated nuclear materials. *Journal of Nuclear Materials*, 462:374 – 381, 2015.

[7] Takashi Tanno, Makoto Fukuda, Shuhei Nogami, and Akira Hasegawa. Microstructure development in neutron irradiated tungsten alloys. *MATERIALS TRANSACTIONS*, 52(7):1447–1451, 2011.

[8] F. Hofmann, D.R. Mason, J.K. Eliason, A.A. Maznev, K.A. Nelson, and S.L. Dudarev. Non-contact measurement of thermal diffusivity in ion-implanted nuclear materials. *Scientific Reports*, 15:16042, 2015.

[9] S.L. Dudarev. Density functional theory models for radiation damage. *Annual Review of Materials Research*, 43:35–61, 2013.

[10] M R Gilbert, S L Dudarev, P M Derlet, and D G Pettifor. Structure and metastability of mesoscopic vacancy and interstitial loop defects in iron and tungsten. *Journal of Physics: Condensed Matter*, 20(34):345214, 2008.

[11] P. M. Derlet, D. Nguyen-Manh, and S. L. Dudarev. Multiscale modeling of crowdion and vacancy defects in body-centered-cubic transition metals. *Phys. Rev. B*, 76:054107, Aug 2007.

[12] A. E. Sand, S. L. Dudarev, and K. Nordlund. High-energy collision cascades in tungsten: Dislocation loops structure and clustering scaling laws. *EPL (Europhysics Letters)*, 103(4):46003, 2013.

[13] X. Yi, A. E. Sand, D. R. Mason, M. A. Kirk, S. G. Roberts, K. Nordlund, and S. L. Dudarev. Direct observation of size scaling and elastic interaction between nano-scale defects in collision cascades. *EPL (Europhysics Letters)*, 110(3):36001, 2015.

[14] W. Jäger and M. Wilkens. Formation of vacancy-type dislocation loops in tungsten bombarded by 60keV Au ions. *Physica Status Solidi (a)*, 32:89–100, 1975.

[15] X. Yi, M.L. Jenkins, M. Briceno, S.G. Roberts, Z. Zhou, and M.A. Kirk. In situ study of self-ion irradiation damage in W and W5Re at 500C. *Philosophical Magazine*, 93(14):1715–1738, 2013.

[16] D.R. Mason, X. Yi, M.A. Kirk, and S.L. Dudarev. Elastic trapping of dislocation loops in cascades in ion-irradiated tungsten foils. *J. Phys.: Condens. Matter*, 26:375701, 2014.

[17] Francesco Ferroni, Xiaoou Yi, Kazuto Arakawa, Steven P. Fitzgerald, Philip D. Edmondson, and Steve G. Roberts. High temperature annealing of ion irradiated tungsten. *Acta Materialia*, 90:380 – 393, 2015.

[18] M. W. Finnis and J. E. Sinclair. A simple empirical n-body potential for transition metals. *Philosophical Magazine A*, 50(1):45–55, 1984.

[19] M-C Marinica, Lisa Ventelon, M R Gilbert, L Proville, S L Dudarev, J Marian, G Bencteux, and F Willaime. Interatomic potentials for modelling radiation defects and dislocations in tungsten. *Journal of Physics: Condensed Matter*, 25(39):395502, 2013.

[20] M. Muzyk, D. Nguyen-Manh, K. J. Kurzydłowski, N. L. Baluc, and S. L. Dudarev. Phase stability, point defects, and elastic properties of W-V and W-Ta alloys. *Phys. Rev. B*, 84:104115, Sep 2011.

[21] G.J. Ackland and R. Thetford. An improved n-body semi-empirical model for body-centred cubic transition metals. *Philosophical Magazine A*, 56:15–30, 1987.

[22] J. Fikar and R. Schublin. Molecular dynamics simulation of radiation damage in bcc tungsten. *Journal of Nuclear Materials*, 386388:97 – 101, 2009. Fusion Reactor MaterialsProceedings of the Thirteenth International Conference on Fusion Reactor Materials.

[23] J.F. Ziegler, J.P. Biersack, and U. Littmark. *The stopping and range of ions in solids*. Pergamon, 1982.

[24] P. Olsson, C. S. Becquart, and C. Domain. Ab initio threshold displacement energies in iron. *Materials Research Letters*, 4(4):219–225, 2016.

[25] G. Kresse and J. Hafner. Ab initio. *Phys. Rev. B*, 47:558–561, Jan 1993.

[26] G. Kresse and J. Furthmüller. Efficient iterative schemes for ab initio total-energy calculations using a plane-wave basis set. *Phys. Rev. B*, 54:11169–11186, Oct 1996.

[27] G. Kresse and J. Furthmller. Efficiency of ab-initio total energy calculations for metals and semiconductors using a plane-wave basis set. *Computational Materials Science*, 6(1):15 – 50, 1996.

[28] John P. Perdew, Kieron Burke, and Matthias Ernzerhof. Generalized gradient approximation made simple. *Phys. Rev. Lett.*, 77:3865–3868, Oct 1996.

[29] Duc Nguyen-Manh and S.L. Dudarev. Trapping of he clusters by inert-gas impurities in tungsten: First-principles predictions and experimental validation. *Nuclear Instruments and Methods in Physics Research Section B: Beam Interactions with Materials and Atoms*, 352:86 – 91, 2015. Proceedings of the 12th International Conference on Computer Simulation of Radiation Effects in Solids, Alacant, Spain, 8-13 June, 2014.

[30] J. N. Mundy. Electrical resistivity-temperature scale of tungsten. *Philosophical Magazine A*, 46(2):345–349, 1982.

[31] P. Ehrhart, P. Jung, H. Schultz, and H. Ullmaier. *Atomic Defects in Metals*, volume 25. Springer-Verlag, Berlin, 1991.

[32] J. Y. Park, H. C. W. Huang, R. W. Siegel, and R. W. Balluffi. A quantitative study of vacancy defects in quenched tungsten by combined field-ion microscopy and electrical resistometry. *Philosophical Magazine A*, 48(3):397–419, 1983.

[33] T. Ahlgren, K. Heinola, N. Juslin, and A. Kuronen. Bond-order potential for point and extended defect simulations in tungsten. *Journal of Applied Physics*, 107(3):033516, 2010.

[34] Zhang Bangwei, Ouyang Yifang, Liao Shuzhi, and Jin Zhanpeng. An analytic MEAM model for all BCC transition metals. *Physica B: Condensed Matter*, 262(34):218 – 225, 1999.

[35] H. C. Kang and W. H. Weinberg. Dynamic Monte Carlo with a proper energy barrier: Surface diffusion and two-dimensional domain ordering. *The Journal of Chemical Physics*, 90(5):2824–2830, 1989.

[36] J.N Mundy, S.T. Ockers, and L.C. Smedskjaer. Vacancy migration enthalpy in tungsten at high temperatures. *Mater. Sci. For.*, 15-18:199–204, 1987.

[37] K-D. Rasch, R. W. Siegel, and H. Schultz. Quenching and recovery investigations of vacancies in tungsten. *Philosophical Magazine A*, 41(1):91–117, 1980.

[38] F.R. de Boer, R. Boom, W.C.M. Mattens, A.R. Miedema, and A.K. Niessen. *Cohesion in Metals*. North-Holland, Amsterdam, 1988.

[39] L. Vitos, A.V. Ruban, H.L. Skriver, and J. Kollr. The surface energy of metals. *Surface Science*, 411(12):186 – 202, 1998.

[40] M. Mrovec, R. Gröger, A. G. Bailey, D. Nguyen-Manh, C. Elsässer, and V. Vitek. Bond-order potential for simulations of extended defects in tungsten. *Phys. Rev. B*, 75:104119, Mar 2007.

[41] N. Juslin, P. Erhart, P. Trskelin, J. Nord, K. O. E. Henriksson, K. Nordlund, E. Salonen, and K. Albe. Analytical interatomic potential for modeling nonequilibrium processes in the WCH system. *Journal of Applied Physics*, 98(12):123520, 2005.

[42] M. K. Debe and David A. King. Space-group determination of the low-temperature W001($\sqrt{2} \times \sqrt{2}$)$r45°$ surface structure by low-energy-electron diffraction. *Phys. Rev. Lett.*, 39:708–711, Sep 1977.

[43] K. Heinola and T. Ahlgren. First-principles study of H on the reconstructed W(100) surface. *Phys. Rev. B*, 81:073409, Feb 2010.

[44] Graeme Henkelman, Gísli Jóhannesson, and Hannes Jónsson. *Methods for Finding Saddle Points and Minimum Energy Paths*, pages 269–302. Springer Netherlands, Dordrecht, 2002.

[45] D R Mason, R E Rudd, and A P Sutton. Atomistic modelling of diffusional phase transformations with elastic strain. *Journal of Physics: Condensed Matter*, 16(27):S2679, 2004.

[46] Haixuan Xu, Yury N. Osetsky, and Roger E. Stoller. Simulating complex atomistic processes: On-the-fly kinetic Monte Carlo scheme with selective active volumes. *Phys. Rev. B*, 84:132103, Oct 2011.

[47] A.B. Bortz, M.H. Kalos, and J.L. Lebowitz. A new algorithm for Monte Carlo simulation of Ising spin systems. *Journal of Computational Physics*, 17(1):10 – 18, 1975.

[48] C.S. Becquart, C. Domain, U. Sarkar, A. DeBacker, and M. Hou. Microstructural evolution of irradiated tungsten: Ab initio parameterisation of an OKMC model. *Journal of Nuclear Materials*, 403(13):75 – 88, 2010.

[49] G Bonny, P Grigorev, and D Terentyev. On the binding of nanometric hydrogenhelium clusters in tungsten. *Journal of Physics: Condensed Matter*, 26(48):485001, 2014.

A Parameterization

The full potential is defined by the energy for atom i (equation 1).

$$E_i = \frac{1}{2} \sum_{j \in \mathcal{N}_i} V(r_{ij}) + F\left[\rho_i\right], \tag{5}$$

The potential can be considered as a piecewise polynomials, smoothly transforming to non-polynomial forms. Start by writing the polynomial switching

function which switches from 0 for $x \leq a$ to 1 for $x \geq b$ and is smooth in first and second derivatives.

$$P(x;a,b) = \begin{cases} 0 & x \leq a \\ \left(\frac{b-x}{b-a}\right)^3 \left(10 - \left(\frac{b-x}{b-a}\right)\left(15 - 6\left(\frac{b-x}{b-a}\right)\right)\right) & a \leq x \leq b \\ 1 & x \geq b \end{cases} . \quad (6)$$

Note that $P(x;b,a) = 1 - P(x;a,b)$.

where $\mathcal{N}_i$ denotes the atoms within the cutoff range $d = 4.400224\mathring{A}$, and

$$\begin{aligned} V(r) &= \left(\sum_k v_k r^k + \Theta\left(b_0 - r\right)\, B\left(b_0 - r\right)^3 \exp(-\alpha r)\right) P(r;r_1,r_2) + V_{\mathrm{ZBL}}(r)\, P(r;r_2,r_1) \\ \rho &= \sum_{j \in \mathcal{N}_i} \sum_k \phi_k r_{ij}^k \\ F[\rho] &= \left(\sum_k f_k \rho^k\right) P(\rho;\rho_1,\rho_2) - \tilde{A}(\sqrt{\rho} - \rho)\, P(\rho;\rho_2,\rho_1) \end{aligned} \quad (7)$$

The polynomial-exponential term in the pairwise potential is the Ackland-Thetford correction, and $V_{\mathrm{ZBL}}(r)$ the ZBL universal screening potential. The ZBL form is given by[23]

$$V_{\mathrm{ZBL}}\left(r\right) = \frac{Z^2}{4\pi\epsilon_0 r}\left[\begin{array}{l} 0.1818\exp(-3.2r/a_s) + 0.5099\exp(-0.9423r/a_s) \\ +0.2802\exp(-0.4029r/a_s) + 0.02817\exp(-0.2016r/a_s) \end{array}\right]. \quad (8)$$

The polynomial coefficients (together with their piecewise ranges) and the other parameters are given in table A. We have cast the parameterization in a gauge where $\rho = 1$ is the equilibrium level and $F[0] = F[1] = 0$. This choice facilitates the construction of alloy or multicomponent potentials[49].

	polynomial coeff				
pairwise	$r \leq r_3$	$r_3 \leq r \leq r_4$	$r_4 \leq r \leq r_5$	$r_5 \leq r \leq r_6$	$r_6 \leq r \leq d$
v_0	485.20687337	1672.80727767	484.70687337	-269633.03766600	-13.15286569
v_1	-657.05630058	-3259.54335870	-657.05630058	521427.92332378	5.97827097
v_2	331.99799706	2597.12562159	331.99799706	-429337.75697398	-0.67931439
v_3	-74.41886462	-1052.88021959	-74.41886462	194931.24632733	0.00000000
v_4	6.25419986	215.98823915	6.25419986	-52643.36541543	0.00000000
v_5	0.00000000	-17.84970547	0.00000000	8443.10885188	0.00000000
v_6	0.00000000	0.00000000	0.00000000	-743.04140840	0.00000000
v_7	0.00000000	0.00000000	0.00000000	27.59876548	0.00000000
density	$r \leq d$				
ϕ_0	0.621131682				
ϕ_1	-0.28231821				
ϕ_2	0.032079982				
embedding	$\rho \leq \rho_-$	$\rho \geq \rho_-$			
f_0	0.00000000	-2.98221766			
f_1	-769.383288570	2.85858359			
f_2	362.5771731	0.00000000			
f_3	-54.09612738	0.00000000			
	non-polynomial parameters				
A-T					
b_0	2.74114361				
B	89.7				
α	2.0				
ZBL					
Z	74				
a_s	0.078908				
	piecewise ranges				
r_1	1.0				
r_2	1.5				
r_3	2.0				
r_4	2.7				
r_5	3.1652				
r_6	3.52				
d	4.400224				
ρ_-	0.15708365				
ρ_1	0.73783958				
ρ_2	0.99447943				

Table 5: Polynomial coefficients, non-polynomial parameters, and piecewise ranges for their applicability. Note that $V(r > d) = 0$. All units $eV, \mathring{A}$.